

Machine learning based non-Newtonian fluid model with molecular fidelity

Huan Lei,^{1,*} Lei Wu,^{2,†} and Weinan E^{2,‡}

¹*Department of Computational Mathematics,
Science & Engineering and Department of Statistics & Probability,
Michigan State University, MI 48824, USA*

²*Department of Mathematics and Program in Applied and Computational Mathematics,
Princeton University, NJ 08544, USA*

Abstract

We introduce a machine-learning-based framework for constructing continuum non-Newtonian fluid dynamics model directly from a micro-scale description. Polymer solution is used as an example to demonstrate the essential ideas. To faithfully retain molecular fidelity, we establish a micro-macro correspondence via a set of encoders for the micro-scale polymer configurations and their macro-scale counterparts, a set of nonlinear conformation tensors. The dynamics of these conformation tensors can be derived from the micro-scale model and the relevant terms can be parametrized using machine learning. The final model, named the deep non-Newtonian model (DeePN²), takes the form of conventional non-Newtonian fluid dynamics models, with a new form of the objective tensor derivative. Numerical results demonstrate the accuracy of DeePN².

* leihuan@msu.edu

† leiwu@princeton.edu

‡ weinan@math.princeton.edu

Accurate modeling of non-Newtonian fluid flows has been a long-standing problem. Existing hydrodynamic models have to resort to ad hoc assumptions either directly at the macro-scale level when writing down constitutive laws, or as closure assumptions when deriving macro-scale models from some underlying micro-scale description. A variety of empirical constitutive models of both integral and derivative types have been developed, including Oldroyd-B [1], Giesekus [2], finite extensible nonlinear elastic Peterlin (FENE-P) [3, 4], Rivlin-Sawyers [5]. These models are designed such that proper frame-indifference is satisfied, but otherwise left with few physical constraints. Despite their broad applications, the robustness and universal applicability of these models are still in doubt. In principle, viscoelastic effects are determined by the polymer configuration distribution, which can be obtained by directly solving the micro-scale Fokker-Planck equation coupled with the macro-scale hydrodynamic equation [6]. However, the cost of such an approach becomes prohibitive for large scale simulations. Several alternative approaches [7–9] based on sophisticated coupling between the micro- and macro-scale models have been proposed. However, the efficiency and accuracy of these approaches rely on a separation between the relevant macro- and micro-scales, something that does not usually happen in practice.

Following recent successes in applying machine learning to constructing reduced dynamics of complex systems [10–17], we present a machine-learning-based approach for constructing admissible and accurate non-Newtonian hydrodynamic models, the deep non-Newtonian model (DeePN²), directly from a micro-scale molecular level description. The challenge lies in formulating the micro-macro correspondence in a natural way, as well as formulating the reduced dynamics and designing deep neural network (DNN) models that simultaneously retain molecular fidelity and physical symmetries. A second challenge is the model interpretability, a well-known weakness of machine-learning-based models. In addition, noises in the data, for example due to thermal fluctuations, also present a challenge.

In DeePN², we construct a set of nonlinear encoder functions directly from micro-scale simulation results, which can be viewed as the “features” of sub-grid polymer configurations. These encoders are used to construct macro-scale conformation tensors which can then be used in the construction of the constitutive laws. The second idea is to formulate the ansatz of reduced dynamics directly from the micro-scale Fokker-Planck equation. Thirdly, we propose a general symmetry-preserving DNN structure to represent the terms in the reduced dynamics. All these are done in an end-to-end fashion, by simultaneously

learning the micro-scale encoders, the polymer stress, and the evolution dynamics in terms of the macro-scale conformation tensors. The conformation tensors are a natural extension of the end-end orientation tensor used in classical rheological models. New forms of objective tensor derivatives naturally arise in this way. The terms for these derivatives can be systematically constructed with clear micro-scale interpretation. Numerical results demonstrate the accuracy of this machine-learning-based model as well as the crucial role of the constructed tensor derivatives encoded with molecular structure.

Let us start with the continuum level description of the dynamics of incompressible non-Newtonian flow in the following generalized form

$$\begin{aligned}\nabla \cdot \mathbf{u} &= 0 \\ \rho \frac{d\mathbf{u}}{dt} &= -\nabla p + \nabla \cdot (\boldsymbol{\tau}_s + \boldsymbol{\tau}_p) + \mathbf{f}_{\text{ext}},\end{aligned}\tag{1}$$

where ρ , \mathbf{u} and p represent the fluid density, velocity and pressure field, respectively. \mathbf{f}_{ext} is the external body force and $\boldsymbol{\tau}_s$ is the solvent stress tensor with shear viscosity η_s , which is assumed to take the Newtonian form $\boldsymbol{\tau}_s = \eta_s(\nabla \mathbf{u} + \nabla \mathbf{u}^T)$. $\boldsymbol{\tau}_p$ is the polymer stress tensor whose constitutive law is generally unknown. To close Eq. (1), traditional models, e.g., Oldroyd-B, Giesekus, and FENE-P, are generally based on the approximation of $\boldsymbol{\tau}_p$ in terms of an empirically chosen conformation tensor (e.g., the end-end orientation tensor), along with some heuristic closure assumption for the dynamics of such a tensor.

To map the microscopic model to the continuum model (1), we assume that (I) the polymer solution can be treated as nearly incompressible on the continuum scale; and (II) the polymer solution is semi-dilute, i.e., the polymer stress $\boldsymbol{\tau}_p$ is dominated by intramolecular interaction $V_b(r)$, where $r = |\mathbf{r}|$ and \mathbf{r} is the end-end vector between the two beads of a dumbbell molecule. Accordingly, the instantaneous $\boldsymbol{\tau}_p$ can be determined by the probability density function $\rho(\mathbf{r}, t)$. We seek for a micro-macro correspondence that directly maps the polymer configurations to a set of conformation tensors, with which we construct the stress model of $\boldsymbol{\tau}_p$ and their evolution dynamics, i.e.,

$$\boldsymbol{\tau}_p = \mathbf{G}(\mathbf{c}_1, \mathbf{c}_2, \dots, \mathbf{c}_n)\tag{2a}$$

$$\frac{D\mathbf{c}_i}{Dt} = \mathbf{H}_i(\nabla \mathbf{u}, \mathbf{c}_1, \dots, \mathbf{c}_n)\tag{2b}$$

$$\mathbf{c}_i = \langle \mathbf{B}_i(\mathbf{r}) \rangle \quad \mathbf{B}_i = \mathbf{f}_i(\mathbf{r})\mathbf{f}_i^T(\mathbf{r}) \quad i = 1, 2, \dots, n\tag{2c}$$

where $\mathbf{c}_i \in \mathbb{R}^{3 \times 3}$ represents the i -th conformation tensor of the polymer configurations

within the local volume unit. It has an explicit micro-scale interpretation — the average of the i -th second-order encoder tensor \mathbf{B}_i with respect to the encoder vector $\mathbf{f}_i(\mathbf{r}) : \mathbb{R}^3 \rightarrow \mathbb{R}^3$. $\frac{\mathcal{D}\mathbf{c}_i}{\mathcal{D}t}$ represents a generalized tensor derivative whose detailed formulation will be discussed later. $\mathbf{G} : \mathbb{R}^{3 \times 3 \times n} \rightarrow \mathbb{R}^{3 \times 3}$ and $\mathbf{H}_i : \mathbb{R}^{3 \times 3 \times n} \rightarrow \mathbb{R}^{3 \times 3}$ are functions that need to be modeled.

One reason for the choice of $\mathbf{B}_i(\mathbf{r})$ is as follows. As the input of the stress model $\mathbf{G}(\cdot)$, $\mathbf{B}_i(\mathbf{r})$ needs to retain rotational symmetry in accordance with the polymer configuration \mathbf{r} . For example, the vector form of $\mathbf{B}_i(\mathbf{r})$ needs to satisfy $\mathbf{B}_i(\mathbf{Q}\mathbf{r}) = \mathbf{Q}\mathbf{B}_i(\mathbf{r})$ for any unitary matrix \mathbf{Q} . This yields $\langle \mathbf{B}_i(\mathbf{r}) \rangle \equiv 0$ (see Appendix). A simple non-trivial choice is a second-order tensor function taking the form of Eq. (2c), so that $\mathbf{B}_i(\mathbf{r})$ satisfies $\mathbf{B}_i(\mathbf{Q}\mathbf{r}) = \mathbf{Q}\mathbf{B}_i(\mathbf{r})\mathbf{Q}^T$ and rotational symmetry of $\mathbf{G}(\cdot)$ can be imposed accordingly.

Model (2) aims at extracting a set of “features” of the configurations, represented by the micro-scale encoder $\{\mathbf{f}_i\}_{i=1}^n$ and the macro-scale conformation tensor $\{\mathbf{c}_i\}_{i=1}^n$, such that the polymer stress $-\langle \mathbf{r} \nabla V_b(\mathbf{r})^T \rangle$ can be well approximated by $\mathbf{G}(\cdot)$ and the evolution of $\{\mathbf{c}_i\}_{i=1}^n$ can be modeled by $\{\mathbf{H}_i(\cdot)\}_{i=1}^n$ self-consistently. As a special case, if $n = 1$ and $\mathbf{f}_1(\mathbf{r}) = \mathbf{r}$, \mathbf{c}_1 recovers the end-end orientation tensor and the stress model recovers the aforementioned rheological models (e.g., Hookean, FENE-P) under special choices of $\mathbf{G}(\cdot)$. In practice, to accurately capture the nonlinear effects in V_b , multiple nonlinear conformation moments are needed.

One important constraint comes from rotational symmetry. Let $\tilde{\mathbf{r}} = \mathbf{Q}\mathbf{r}$, where \mathbf{Q} is unitary. We must have

$$\mathbf{f}_i(\tilde{\mathbf{r}}) = \mathbf{Q}\mathbf{f}_i(\mathbf{r}) \quad (3a)$$

$$\mathbf{G}(\tilde{\mathbf{c}}_1, \dots, \tilde{\mathbf{c}}_n) = \mathbf{Q}\mathbf{G}(\mathbf{c}_1, \dots, \mathbf{c}_n)\mathbf{Q}^T \quad (3b)$$

$$\mathbf{H}_i(\tilde{\mathbf{c}}_1, \dots, \tilde{\mathbf{c}}_n) = \mathbf{Q}\mathbf{H}_i(\mathbf{c}_1, \dots, \mathbf{c}_n)\mathbf{Q}^T \quad (3c)$$

where $\tilde{\mathbf{c}}_i = \mathbf{Q}\mathbf{c}_i\mathbf{Q}^T$. For the tensor derivative $\mathcal{D}\mathbf{c}_i/\mathcal{D}t$, we should have

$$\widetilde{\frac{\mathcal{D}\mathbf{c}_i}{\mathcal{D}t}} = \mathbf{Q} \frac{\mathcal{D}\mathbf{c}_i}{\mathcal{D}t} \mathbf{Q}^T \quad i = 1, 2, \dots, n \quad (4)$$

This constraint is satisfied by the various objective tensor derivatives in most existing rheological models, such as the upper-convected [18], the covariant [18] and the Zaremba-Jaumann [19] derivatives, but these forms are not suitable for us since they lack the desired accuracy. Fortunately these constraints are satisfied automatically if we formulate our macro-scale model based on the underlying micro-scale model.

We start from the Fokker-Planck equation [20],

$$\frac{\partial \rho(\mathbf{r}, t)}{\partial t} = -\nabla \cdot \left[(\boldsymbol{\kappa} \cdot \mathbf{r})\rho - \frac{2k_B T}{\gamma} \nabla \rho - \frac{2}{\gamma} \nabla V_b(r)\rho \right], \quad (5)$$

where $k_B T$ is the thermal energy, γ is the friction coefficient coupled with solvent and $\boldsymbol{\kappa} := \nabla \mathbf{u}^T$ is the strain of the fluid. Accordingly, the evolution of \mathbf{c}_i is given by

$$\frac{d}{dt} \mathbf{c}_i - \boldsymbol{\kappa} : \langle \mathbf{r} \nabla_{\mathbf{r}} \otimes \mathbf{B}_i(\mathbf{r}) \rangle = \frac{2k_B T}{\gamma} \langle \nabla_{\mathbf{r}}^2 \mathbf{B}_i(\mathbf{r}) \rangle + \frac{2}{\gamma} \langle \nabla V_b(r) \cdot \nabla_{\mathbf{r}} \mathbf{B}_i(\mathbf{r}) \rangle, \quad (6)$$

where $:$ is the double-dot product. It is easy to see that Eqs. (6) and (5) are rotationally invariant (see detailed proof in Appendix). Therefore, we can write: $\mathcal{D}\mathbf{c}_i/\mathcal{D}t$ and $\mathbf{H}_i(\cdot)$:

$$\frac{\mathcal{D}\mathbf{c}_i}{\mathcal{D}t} = \frac{d}{dt} \mathbf{c}_i - \boldsymbol{\kappa} : \mathcal{E}_i \quad (7a)$$

$$\mathbf{H}_i = \frac{2k_B T}{\gamma} \mathbf{H}_{1,i} + \frac{2}{\gamma} \mathbf{H}_{2,i} \quad (7b)$$

where

$$\begin{aligned} \mathcal{E}_i(\mathbf{c}_1, \dots, \mathbf{c}_n) &= \langle \mathbf{r} \nabla_{\mathbf{r}} \otimes \mathbf{B}_i(\mathbf{r}) \rangle \\ \mathbf{H}_{1,i}(\mathbf{c}_1, \dots, \mathbf{c}_n) &= \langle \nabla_{\mathbf{r}}^2 \mathbf{B}_i(\mathbf{r}) \rangle \\ \mathbf{H}_{2,i}(\mathbf{c}_1, \dots, \mathbf{c}_n) &= \langle \nabla V_b(r) \cdot \nabla_{\mathbf{r}} \mathbf{B}_i(\mathbf{r}) \rangle \end{aligned} \quad (8)$$

\mathcal{E}_i is a 4-th order tensor function and $\mathbf{H}_{1,i}$, $\mathbf{H}_{2,i}$ are 2nd order tensor functions. They will be approximately represented by DNNs.

Note that $\mathcal{D}\mathbf{c}_i/\mathcal{D}t$ depends on \mathcal{E}_i , which encodes some micro-scale information from $\mathbf{B}_i(\mathbf{r})$. This is different from the common choices of the objective tensor derivatives in existing models. As shown in the numerical examples, such a formulation that faithfully accounts for the micro-scale polymer configuration is crucial for the accuracy of the constitutive model for \mathbf{c}_i .

Special rotation-symmetry-preserving DNNs are needed for the encoder functions $\{\mathbf{f}_i\}_{i=1}^n$, the 2nd order tensors \mathbf{G} and $\{\mathbf{H}_{1,i}, \mathbf{H}_{2,i}\}_{i=1}^n$ and the 4th order tensors $\{\mathcal{E}_i\}_{i=1}^n$ such that the symmetry conditions (3) and (4) are satisfied. For Eq. (3a) to hold, one can show that $\mathbf{f}_i(\mathbf{r})$ has to take the form

$$\mathbf{f}_i(\mathbf{r}) = g_i(r) \mathbf{r}, \quad (9)$$

where $g_i(r)$ is a scalar encoder function (see Appendix). We always set $g_1(r) \equiv 1$, yielding $\mathbf{G} \propto \mathbf{H}_{2,1}$.

To construct the DNNs for \mathbf{G} and $\{\mathbf{H}_{1,i}, \mathbf{H}_{2,i}\}_{i=1}^n$ that satisfy Eq. (3c), we can transform $\{\mathbf{c}_i\}_{i=1}^n$ into a fixed frame for the DNN input. One natural choice is the eigen-space of the conformation tensor $\mathbf{c}_1 = \langle \mathbf{r}\mathbf{r}^T \rangle$. Let \mathbf{V} be the matrix composed of the eigenvectors of \mathbf{c}_1 . Define

$$\begin{aligned}\mathbf{H}_{j,i}(\mathbf{c}_1, \dots, \mathbf{c}_n) &= \mathbf{V} \hat{\mathbf{H}}_{j,i}(\hat{\mathbf{c}}_1, \dots, \hat{\mathbf{c}}_n) \mathbf{V}^T \\ \hat{\mathbf{c}}_i &= \mathbf{V}^T \mathbf{c}_i \mathbf{V} \quad j = 1, 2 \quad i = 1, \dots, n\end{aligned}\tag{10}$$

$\hat{\mathbf{c}}_1$ is a diagonal matrix composed of the eigenvalues of \mathbf{c}_1 . The DNNs will be constructed to learn $\hat{\mathbf{H}}_{j,i}$.

The learning of the 4th order tensors $\{\mathcal{E}_i\}_{i=1}^n$ is based on the following decomposition:

$$\mathcal{E}_i(\mathbf{c}_1, \dots, \mathbf{c}_n) = \langle g_i(r)^2 \mathbf{r} \nabla_{\mathbf{r}} \otimes \mathbf{r} \mathbf{r}^T \rangle + \sum_{k=1}^6 \mathbf{E}_{1,i}^{(k)}(\mathbf{c}_1, \dots, \mathbf{c}_n) \otimes \mathbf{E}_{2,i}^{(k)}(\mathbf{c}_1, \dots, \mathbf{c}_n).\tag{11}$$

$\mathbf{E}_{1,i}, \mathbf{E}_{2,i} \in \mathbb{R}^{3 \times 3}$ are second-order tensors satisfying the rotational symmetry condition similar to Eq. (3c), i.e.,

$$\begin{aligned}\mathbf{E}_{1,i}(\tilde{\mathbf{c}}_1, \dots, \tilde{\mathbf{c}}_n) &= \mathbf{Q} \mathbf{E}_{1,i}(\mathbf{c}_1, \dots, \mathbf{c}_n) \mathbf{Q}^T \\ \mathbf{E}_{2,i}(\tilde{\mathbf{c}}_1, \dots, \tilde{\mathbf{c}}_n) &= \mathbf{Q} \mathbf{E}_{2,i}(\mathbf{c}_1, \dots, \mathbf{c}_n) \mathbf{Q}^T.\end{aligned}\tag{12}$$

It is shown in Appendix that this decomposition satisfies Eq. (4). Accordingly, \mathcal{E}_i can be constructed by a set of second order tensors $\mathbf{E}_{1,i}$ and $\mathbf{E}_{2,i}$, which can be constructed similar to Eq. (10). Note that with this form, the first term in the RHS of Eq. (11) becomes $\boldsymbol{\kappa} \mathbf{c}_i + \mathbf{c}_i \boldsymbol{\kappa}^T$ similar to the upper-convected derivative. In summary, the DNNs are designed to parametrize $\{g_i(r)\}_{i=2}^n, \{\hat{\mathbf{H}}_{1,i}, \hat{\mathbf{H}}_{2,i}, \hat{\mathcal{E}}_i\}_{i=1}^n$.

Finally, the DNNs are trained by minimizing the loss

$$L = \lambda_{H_1} L_{H_1} + \lambda_{H_2} L_{H_2} + \lambda_{\mathcal{E}} L_{\mathcal{E}},\tag{13}$$

where L_{H_1} , L_{H_2} and $L_{\mathcal{E}}$ are the empirical risk associated with $\{\mathbf{H}_{1,i}\}_{i=1}^n$, $\{\mathbf{H}_{2,i}\}_{i=1}^n$ and $\{\mathcal{E}_i\}_{i=1}^n$ respectively. λ_{H_1} , λ_{H_2} and $\lambda_{\mathcal{E}}$ are hyper-parameters (see Appendix). Note that the encoders $\{g_i(r)\}_{i=2}^n$ do not explicitly appear in L ; they are trained through the learning of $\hat{\mathbf{H}}$ and \mathcal{E} .

The DeePN² model is made up of Eqs. (1) and (2). Note that the model takes the form of classical empirical models. The only differences are that some new conformation tensors and a new form of objective tensor derivative are introduced, and some of the terms in the

equations are represented as function subroutines in the form of NN models. The latter is no different from the situation commonly found in gas dynamics, where the equations of state for complex gases are given as tables or function subroutines.

To demonstrate the model accuracy, we consider a polymer solution with polymer number density $n_p = 0.5$. The bond potential $V_b(r)$ is chosen to be FENE

$$V_b(r) = -\frac{k_s}{2}r_0^2 \log \left[1 - \frac{r^2}{r_0^2} \right], \quad (14)$$

where k_s is the spring constant. r_0 is the maximum bond extension. The continuum model is constructed using $n = 3$ encoder functions extracted from the microscopic polymer configurations. We also experimented with larger values of n but did not see appreciable improvement. That been said, the choice of n needs to be looked into more carefully in the future.

The training data set is collected from molecular dynamics (MD) simulations under different shear rate (see Appendix). Fig. 1 shows the encoder functions $g(r)$ with $r_0 = 2.4$, $k_s = 0.1$. To validate the DeePN² model, we consider a quasi-equilibrium dynamics of the polymer solution with $k_B T = 0.25$, while the initial polymer configuration is taken from the equilibrium state with $k_B T = 0.6$. The relaxation process is simulated using both MD and DeepN². Fig. 1 shows the evolution of the trace of \mathbf{c}_1 and $\boldsymbol{\tau}_p$. The predictions from DeePN² agree well with the MD results. For comparison, we also simulate the relaxation process using the Oldroyd-B (i.e., Hookean) and FENE-P model, where the model parameters are chosen such that the initial conditions of \mathbf{c}_1 and $\boldsymbol{\tau}_p$ match the MD results. One can see clear deviations.

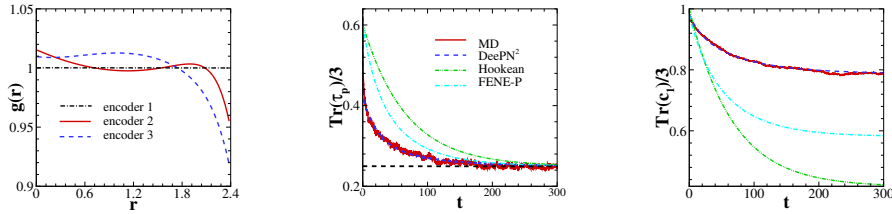


FIG. 1. Quasi-equilibrium relaxation process obtained from direct MD simulation, the present DeePN², canonical Hookean and FENE-P model. Left: Encoder function $g(r)$. Middle: Evolution of $\boldsymbol{\tau}_p$. Right: Evolution of $\mathbf{c}_1 = \langle \mathbf{r}\mathbf{r}^T \rangle$.

Next, we consider the non-equilibrium process of a reverse Poiseuille flow (RPF) in a

domain $[0, 40] \times [0, 80] \times [0, 40]$ (reduced unit), with periodic boundary condition imposed in each direction. Starting from $t = 0$, an external field $\mathbf{f}_{\text{ext}} = (f_b, 0, 0)$ is applied in the region $y < 40$ and an opposite field $\mathbf{f}_{\text{ext}} = (-f_b, 0, 0)$ is applied in the region $y > 40$. Fig. 2 shows the instantaneous velocity profiles with $r_0 = 3.8$ and $f_b = 0.02$. The predictions from DeePN² agree well with the MD results while FENE-P yields apparent deviations. Furthermore, Fig. 2 shows the velocity evolution at $y = 6$ and $y = 14$. The predictions from the Hookean and FENE-P models show pronounced overestimations on both the magnitude and duration of the oscillation behavior. Such limitations of the FENE-P model have already been noted in Ref. [7]. From the microscopic perspective, the discrepancy arises from the mean field approximation, $\boldsymbol{\tau}_p \approx \mathbf{c}/(1 - \text{Tr}(\mathbf{c})/r_0^2)$. Such an approximation cannot capture the nonlinear response when individual polymer bond length approaches r_0 . In contrast, DeePN² can capture such microscale “bond length dispersion” via the additional macroscale nonlinear conformation tensors $\mathbf{c}_2, \dots, \mathbf{c}_n$.

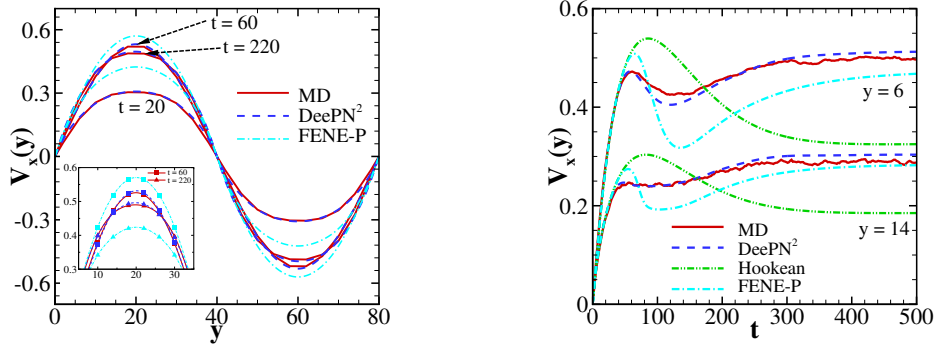


FIG. 2. Evolution of the RPF obtained from MD and various models. Left: velocity profiles at $t = 20, 60, 220$. Right: velocity evolution at $y = 6$ and $y = 14$. The parameters of the Hookean and FENE-P model are chosen such that the equilibrium bond length matches the MD results.

Shown in Fig. 3(a) is the evolution of \mathbf{c}_1 at $y = 6$. The DeePN² faithfully predicts the responses of the polymer configurations under the external flow field. The polymer stress $\boldsymbol{\tau}_p$ are also accurately predicted by the instantaneous conformation tensors, as shown in Fig. 3(b-c). The accuracy on the polymer configuration response and stress tensor under the external field can also be examined by the shear-rate-dependent viscosity. As shown in Fig. 3(d), predictions by DeePN² agree well with the MD results. In contrast, the Hookean and FENE-P models are insufficient for capturing the dynamic responses, leading to apparent

deviations.

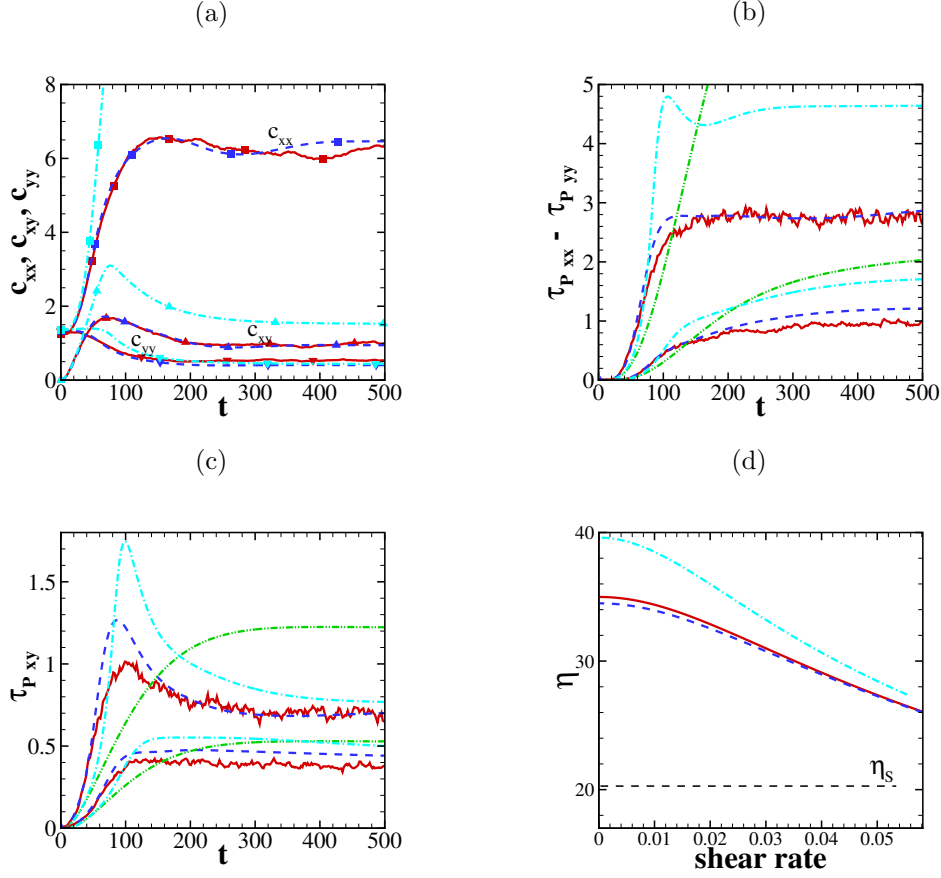


FIG. 3. The micro-macro correspondence during the evolution of the RPF. (a) Evolution of \mathbf{c}_1 at $y = 6$. (b-c) Normal stress difference $\tau_{p_{xx}} - \tau_{p_{yy}}$ and shear stress $\tau_{p_{xy}}$ at $y = 6$ (upper lines) and $y = 14$ (lower lines). (d) Shear-rate-dependent viscosity. Same line scheme as Fig. 2.

Besides the first-principle-based stress model and dynamic closure, another distinctive feature of the DeePN² model is the generalized objective tensor derivative $\mathcal{D}\mathbf{c}_i/\mathcal{D}t$:

$$\frac{\mathcal{D}\mathbf{c}_i}{\mathcal{D}t} = \overset{\nabla}{\mathbf{c}}_i - \boldsymbol{\kappa} : \left[\sum_{k=1}^6 \mathbf{E}_{1,i}^{(k)}(\mathbf{c}_1, \dots, \mathbf{c}_n) \otimes \mathbf{E}_{2,i}^{(k)}(\mathbf{c}_1, \dots, \mathbf{c}_n) \right], \quad (15)$$

where $\overset{\nabla}{\mathbf{c}}_i$ is the standard upper-convected derivative and the second term arises from the source term $\langle \mathbf{r} \nabla_{\mathbf{r}} g(r)^2 \otimes \mathbf{r} \mathbf{r}^T \rangle$ in Eq. (6). Therefore, the second term of $\mathcal{D}\mathbf{c}_i/\mathcal{D}t$ is embedded with the nonlinear response to external field $\boldsymbol{\kappa}$, inherited from the encoder $g_i(r)$. As a numerical test, we use the present model to simulate the RPF, where $\mathcal{D}\mathbf{c}_i/\mathcal{D}t$ is chosen to be the upper-convected derivative $\overset{\nabla}{\mathbf{c}}_i$ and other modeling terms remain the same. Fig. 4

shows the evolution of the velocities and \mathbf{c}_1 . By ignoring the second term in Eq. (15), the predictions show apparent deviations from the MD results. This indicates that the empirical choices of the objective tensor derivative are not accurate. To achieve the desired accuracy, these derivatives have to retain some information from the specific conformation tensor.

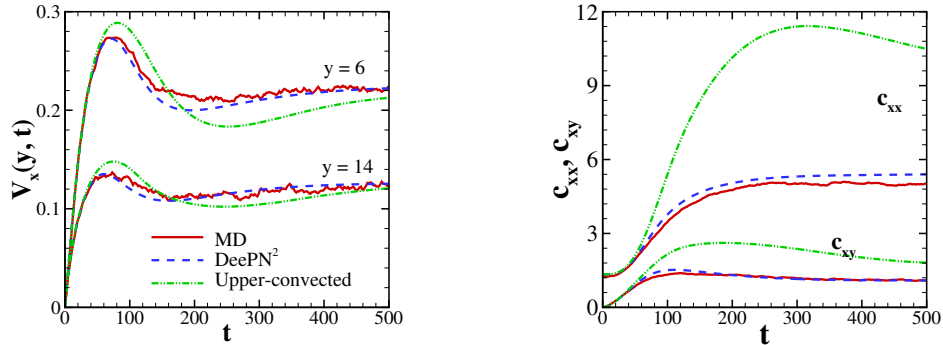


FIG. 4. The effectiveness of the objective tensor derivative constructed by Eq. (15). The additional source term plays a vital role in the accurate modeling of the fluid systems. The model that uses the canonical upper-convected derivative shows apparent deviations from the MD results for the evolution of the velocities (left) and \mathbf{c}_1 (right) at $y = 6$.

In this letter, we presented a machine learning-based approach for constructing hydrodynamic models for polymer fluids, DeePN², directly from the microscale descriptions. While this is only the first step in a long program, the results we obtained have already demonstrated the potential of such an approach for achieving accuracy and efficiency at the same time. The construction is based on an underlying micro-scale model. It respects the symmetries of the underlying physical system. It is end-to-end, and requires little ad hoc human intervention. Contrary to conventional wisdom on machine learning models, the model obtained here is quite interpretable, and in fact shows quite some physical insight. It has already demonstrated much better accuracy than existing hydrodynamic models in several tests.

While we focused on polymer solutions, the present approach is quite general and can be readily adapted to other systems of complex fluids.

It should also be noted that what we discussed is only a first step towards constructing accurate and robust hydrodynamic models for non-Newtonian fluids. Much needs to be done in order to obtain truly reliable hydrodynamic models for these polymer systems. Among

the issues that remain to be addressed, let us mention coupling the training process with the adaptive selection of the training data as was done in MD [21], the automatic choice of the model complexity (e.g. the choice of n), and the improvement of the underlying micro-scale model. While some of these will take time, there is no doubt that machine learning, used in the right way, can help us to tackle the long-standing problem of developing truly reliable hydrodynamic models for complex fluids.

ACKNOWLEDGMENTS

We thank Jiequn Han, Chao Ma, Linfeng Zhang for helpful discussions. The work of Huan Lei is supported in part by the Extreme Science and Engineering Discovery Environment (XSEDE) Bridges at the Pittsburgh Supercomputing Center through allocation DMS190030 and the High Performance Computing Center at Michigan State University. The work of Weinan E and Lei Wu is supported in part by a gift to Princeton University from iFlytek and the ONR grant N00014-13-1-0338.

-
- [1] J. G. Oldroyd and A. H. Wilson, Proceedings of the Royal Society of London. Series A. Mathematical and Physical Sciences **200**, 523 (1950).
 - [2] H. Giesekus, Journal of Non-Newtonian Fluid Mechanics **11**, 69 (1982).
 - [3] A. Peterlin, Journal of Polymer Science Part B: Polymer Letters **4**, 287 (1966).
 - [4] R. Bird, P. Dotson, and N. Johnson, Journal of Non-Newtonian Fluid Mechanics **7**, 213 (1980).
 - [5] R. S. Rivlin and K. N. Sawyers, Annual Review of Fluid Mechanics **3**, 117 (1971).
 - [6] X. J. Fan, Acta Mechanica Sinica **1**, 49 (1989).
 - [7] M. Laso and H. Öttinger, Journal of Non-Newtonian Fluid Mechanics **47**, 1 (1993).
 - [8] M. Hulsen, A. van Heel, and B. van den Brule, Journal of Non-Newtonian Fluid Mechanics **70**, 79 (1997).
 - [9] W. Ren and W. E, Journal of Computational Physics **204**, 1 (2005).
 - [10] C. Ma, J. Wang, and W. E, arXiv preprint arXiv:1808.04258 (2018).
 - [11] P. R. Vlachas, W. Byeon, Z. Y. Wan, T. P. Sapsis, and P. Koumoutsakos, Proceedings of the Royal Society A: Mathematical, Physical and Engineering Sciences **474**, 20170844 (2018).

- [12] J. Han, C. Ma, Z. Ma, and W. E, Proceedings of the National Academy of Sciences **116**, 21983 (2019).
- [13] J. Ling, A. Kurzawski, and J. Templeton, Journal of Fluid Mechanics **807**, 155166 (2016).
- [14] J. X. Wang, J. L. Wu, and H. Xiao, Phys. Rev. Fluids **2**, 034603 (2017).
- [15] B. Lusch, J. N. Kutz, and S. L. Brunton, Nature Communications **9**, 4950 (2018).
- [16] A. J. Linot and M. D. Graham, arXiv preprint arXiv:2001.04263 (2019).
- [17] M. Raissi, A. Yazdani, and G. E. Karniadakis, Science **367**, 1026 (2020).
- [18] J. G. Oldroyd and A. H. Wilson, Proceedings of the Royal Society of London. Series A. Mathematical and Physical Sciences **200**, 523 (1950).
- [19] S. Zaremba, Bull. Int. Acad. Sci. Cracovie , 594 (1903).
- [20] R. B. Bird, C. F. Curtiss, R. C. Armstrong, and O. Hassager, *Dynamics of Polymeric Liquids, Volume 2: Kinetic Theory, 2nd Edition*, 2nd ed. (Wiley, 1987).
- [21] L. Zhang, D.-Y. Lin, H. Wang, R. Car, and W. E, Phys. Rev. Materials **3**, 023804 (2019).

Appendix A: Rotational symmetry of the model ansatz and the DNN representation

In this section, we show that both the modeling ansatz and the DNN representation of the DeePN² model satisfy the rotational invariance condition.

1. Rotational invariance from the continuum and microscopic perspective

Let us consider a symmetric tensor $\mathbf{c} \in \mathbb{R}^{3 \times 3}$ in two different coordinate frames. Frame 1 is a static inertial frame. We let $\tilde{\mathbf{x}}, \tilde{\mathbf{v}} := \mathbf{v}(\tilde{\mathbf{x}}, t)$, $\tilde{\mathbf{c}} := \mathbf{c}(\tilde{\mathbf{x}}, t)$, the position, velocity and \mathbf{c} in frame 1. Framework 2 is a rotated frame which is related to frame 1 by a unitary matrix $\mathbf{Q}(t)$. We denote $\mathbf{x}, \mathbf{v}(\mathbf{x}, t)$, $\mathbf{c}(\mathbf{x}, t)$ the position, velocity and \mathbf{c} in frame 2. Accordingly, \mathbf{x} , \mathbf{c} and \mathbf{v} follows the transformation rule

$$\begin{aligned}\tilde{\mathbf{x}} &= \mathbf{Q}\mathbf{x} \\ \tilde{\mathbf{v}} &= \mathbf{Q}\mathbf{v}(\mathbf{x}, t) + \dot{\mathbf{Q}}\mathbf{Q}^T\tilde{\mathbf{x}} \\ \tilde{\mathbf{c}} &= \mathbf{Q}\mathbf{c}(\mathbf{x}, t)\mathbf{Q}^T\end{aligned}\tag{A1}$$

To construct the dynamics of \mathbf{c} , we need to choose an objective derivative $\frac{\mathcal{D}\mathbf{c}}{\mathcal{D}t}$ which retains proper rotational symmetry, i.e.,

$$\frac{\mathcal{D}\tilde{\mathbf{c}}}{\mathcal{D}t}\bigg|_{\text{frame1}} = \mathbf{Q}(t)\frac{\mathcal{D}\mathbf{c}}{\mathcal{D}t}\bigg|_{\text{frame2}}\mathbf{Q}(t)^T.\tag{A2}$$

For example, if we choose $\mathcal{D}/\mathcal{D}t$ as the material derivative $\frac{d}{dt} := \frac{\partial}{\partial t} + \mathbf{v} \cdot \nabla$, Eq. (A2) cannot be satisfied, since

$$\frac{\mathcal{D}\tilde{\mathbf{c}}}{\mathcal{D}t}\bigg|_{\text{frame1}} = \dot{\mathbf{Q}}\mathbf{c}\mathbf{Q}^T + \mathbf{Q}\mathbf{c}\dot{\mathbf{Q}}^T + \mathbf{Q}\frac{d\mathbf{c}}{dt}\bigg|_{\text{frame1}} = \dot{\mathbf{Q}}\mathbf{c}\mathbf{Q}^T + \mathbf{Q}\mathbf{c}\dot{\mathbf{Q}}^T + \mathbf{Q}\frac{\mathcal{D}\mathbf{c}}{\mathcal{D}t}\bigg|_{\text{frame2}}\mathbf{Q}^T,\tag{A3}$$

where the second identity follows from

$$\begin{aligned}\frac{d\mathbf{c}}{dt}\bigg|_{\text{frame1}} &= \frac{\partial \mathbf{c}(\mathbf{Q}^T\tilde{\mathbf{x}}, t)}{\partial t} + \tilde{\mathbf{v}} \cdot \nabla_{\tilde{\mathbf{x}}}\mathbf{c}(\mathbf{Q}^T\tilde{\mathbf{x}}, t) \\ &= \frac{\partial \mathbf{c}(\mathbf{x}, t)}{\partial t} + \left(\dot{\mathbf{Q}}^T\tilde{\mathbf{x}} \cdot \nabla_{\mathbf{x}}\right)\mathbf{c} + \left(\mathbf{Q}\mathbf{v}(\mathbf{x}, t) + \dot{\mathbf{Q}}\mathbf{x}\right) \cdot \nabla_{\tilde{\mathbf{x}}}\mathbf{c} \\ &= \frac{\partial \mathbf{c}(\mathbf{x}, t)}{\partial t} + \mathbf{v}(\mathbf{x}, t) \cdot \nabla_{\mathbf{x}}\mathbf{c} \\ &= \frac{d\mathbf{c}}{dt}\bigg|_{\text{frame2}}\end{aligned}\tag{A4}$$

Alternatively, if we choose $\mathcal{D}/\mathcal{D}t$ to be the objective tensor derivatives coupled with $\boldsymbol{\kappa} := (\nabla \mathbf{v})^T$, e.g., the upper-convected $\overset{\nabla}{\mathbf{c}} = \frac{d\mathbf{c}}{dt} - \boldsymbol{\kappa}\mathbf{c} - \mathbf{c}\boldsymbol{\kappa}^T$, covariant derivative $\overset{\Delta}{\mathbf{c}} = \frac{d\mathbf{c}}{dt} + \boldsymbol{\kappa}^T\mathbf{c} + \mathbf{c}\boldsymbol{\kappa}$, the Jaumann derivative $\overset{\circ}{\mathbf{c}} = \frac{1}{2}(\overset{\nabla}{\mathbf{c}} + \overset{\Delta}{\mathbf{c}})$, Eq. (A2) is satisfied. For example,

$$\begin{aligned}\overset{\nabla}{\mathbf{c}}|_{\text{frame } 1} &= \dot{\mathbf{Q}}\mathbf{c}\mathbf{Q}^T + \mathbf{Q}\mathbf{c}\dot{\mathbf{Q}}^T + \mathbf{Q}\frac{d\mathbf{c}}{dt}|_{\text{frame } 2}\mathbf{Q}^T \\ &\quad - (\mathbf{Q}\boldsymbol{\kappa}\mathbf{Q}^T + \dot{\mathbf{Q}}\mathbf{Q}^T)\mathbf{Q}\mathbf{c}\mathbf{Q}^T - \mathbf{Q}\mathbf{c}\mathbf{Q}^T(\mathbf{Q}\boldsymbol{\kappa}^T\mathbf{Q}^T + \mathbf{Q}\dot{\mathbf{Q}}^T) \\ &= \mathbf{Q}\frac{d\mathbf{c}}{dt}|_{\text{frame } 2}\mathbf{Q}^T - \mathbf{Q}\boldsymbol{\kappa}\mathbf{c}\mathbf{Q}^T - \mathbf{Q}^T\mathbf{c}\boldsymbol{\kappa}^T\mathbf{Q} \\ &= \mathbf{Q}\overset{\nabla}{\mathbf{c}}|_{\text{frame } 2}\mathbf{Q}^T.\end{aligned}\tag{A5}$$

On the other hand, this analysis does not provide us concrete guidance to constructing $\frac{D\mathbf{c}}{Dt}$, since multiple choices such as $\overset{\nabla}{\mathbf{c}}$, $\overset{\Delta}{\mathbf{c}}$ and $\overset{\circ}{\mathbf{c}}$ all satisfy Eq. (A2). To address this issue, we look for a micro-scale perspective based on the Fokker-Planck equation to understand the rotational invariance and construct $\frac{D\mathbf{c}}{Dt}$.

Let us consider the Fokker-Planck equation of a dumb-bell polymer with end-end vector \mathbf{r} coupled with flow field \mathbf{v} . By ignoring the external field, the evolution of the density $\rho(\mathbf{r}, t)$ is governed by

$$\frac{\partial \rho(\mathbf{r}, t)}{\partial t} = -\nabla \cdot \left[(\boldsymbol{\kappa} \cdot \mathbf{r})\rho - \frac{2k_B T}{\gamma} \nabla \rho - \frac{2}{\gamma} \nabla V_b(r)\rho \right], \tag{A6}$$

where γ is the friction coefficient of the solvent, $V_b(r)$ is the intra-molecule potential energy.

Proposition A.1. *Eq. (A6) retains rotational invariance under the transformation by Eq. (A1), i.e.*

$$\tilde{\rho} := \rho(\tilde{\mathbf{r}}, t)|_{\text{frame } 1} \equiv \rho(\mathbf{r}, t)|_{\text{frame } 2} \tag{A7}$$

Proof.

$$\begin{aligned}\frac{\partial \tilde{\rho}}{\partial t} + \nabla_{\tilde{\mathbf{r}}} \cdot ((\tilde{\boldsymbol{\kappa}} \cdot \tilde{\mathbf{r}}) \tilde{\rho})|_{\text{frame } 1} \\ &= \frac{\partial \rho}{\partial t} + \dot{\mathbf{Q}}^T \tilde{\mathbf{r}} \cdot \nabla_{\mathbf{r}} \rho + \nabla_{\tilde{\mathbf{r}}} \cdot \left((\mathbf{Q}\boldsymbol{\kappa}\mathbf{Q}^T + \dot{\mathbf{Q}}\mathbf{Q}^T) \cdot \mathbf{Q}\rho \right) \\ &= \frac{\partial \rho}{\partial t} + \dot{\mathbf{Q}}^T \mathbf{Q}\mathbf{r} \cdot \nabla_{\mathbf{r}} \rho + \nabla_{\mathbf{r}} \cdot (\boldsymbol{\kappa} \cdot \mathbf{r}\rho) + \nabla_{\mathbf{r}} \cdot (\mathbf{Q}^T \dot{\mathbf{Q}}\mathbf{r}\rho) \\ &\equiv \frac{\partial \rho}{\partial t} + \nabla_{\mathbf{r}} \cdot (\boldsymbol{\kappa} \cdot \mathbf{r}\rho)|_{\text{frame } 2}\end{aligned}\tag{A8}$$

where we have used the fact that $\dot{\mathbf{Q}}^T\mathbf{Q}$ is anti-symmetric. In addition, it is straightforward to show that the terms $\nabla^2 \rho$ and $\nabla \cdot \nabla V_b(r)$ are invariant. Therefore we have (A7). \square

Accordingly, if we define \mathbf{c} to be the mean value of a second-order tensor $\mathbf{B}(\mathbf{r}) : \mathbb{R}^3 \rightarrow \mathbb{R}^{3 \times 3}$, the dynamics follows

$$\frac{d}{dt} \langle \mathbf{B}(\mathbf{r}) \rangle = \boldsymbol{\kappa} : \langle \mathbf{r} \nabla_{\mathbf{r}} \otimes \mathbf{B} \rangle + \frac{2k_B T}{\gamma} \langle \nabla_{\mathbf{r}}^2 \mathbf{B} \rangle + \frac{2}{\gamma} \langle \nabla U(\mathbf{r}) \cdot \nabla_{\mathbf{r}} \mathbf{B} \rangle \quad (\text{A9})$$

Proposition A.2. *If $\mathbf{B}(r)$ obeys rotational symmetry $\tilde{\mathbf{B}} := \mathbf{B}(\mathbf{Q}^T \mathbf{r}) = \mathbf{Q} \mathbf{B} \mathbf{Q}^T$, then so does (A9).*

Proof. Using Eq. (A3), the individual terms in frame 1 follow

$$\frac{d}{dt} \langle \tilde{\mathbf{B}} \rangle \big|_{\text{frame 1}} = \dot{\mathbf{Q}} \langle \mathbf{B} \rangle \mathbf{Q}^T + \mathbf{Q} \langle \mathbf{B} \rangle \dot{\mathbf{Q}}^T + \mathbf{Q} \frac{d}{dt} \langle \mathbf{B} \rangle \big|_{\text{frame 2}} \dot{\mathbf{Q}}^T. \quad (\text{A10})$$

Note that

$$\begin{aligned} \tilde{\boldsymbol{\kappa}} : \langle \tilde{\mathbf{r}} \nabla_{\tilde{\mathbf{r}}} \tilde{\mathbf{B}} \rangle \big|_{\text{frame1}} &= \left[\left(\mathbf{Q} \boldsymbol{\kappa} \mathbf{Q}^T + \dot{\mathbf{Q}} \mathbf{Q}^T \right) \cdot \mathbf{Q} \mathbf{r} \right] \cdot \mathbf{Q} \nabla_{\mathbf{r}} (\mathbf{Q} \mathbf{B} \mathbf{Q}^T) \\ &= (\boldsymbol{\kappa} \cdot \mathbf{r}) \cdot \nabla_{\mathbf{r}} (\mathbf{Q} \mathbf{B} \mathbf{Q}^T) + (\mathbf{Q}^T \dot{\mathbf{Q}} \mathbf{r}) \cdot \nabla_{\mathbf{r}} (\mathbf{Q} \mathbf{B} \mathbf{Q}^T) \\ &= \mathbf{Q} (\boldsymbol{\kappa} \cdot \mathbf{r}) \cdot \nabla_{\mathbf{r}} \mathbf{B} \mathbf{Q}^T + \mathbf{Q} \left(\mathbf{Q}^T \dot{\mathbf{Q}} \mathbf{B} + \mathbf{B} \dot{\mathbf{Q}}^T \mathbf{Q} \right) \mathbf{Q}^T \end{aligned} \quad (\text{A11})$$

where we have used the relation

$$(\mathbf{A} \mathbf{r}) \cdot \nabla \mathbf{B} = \mathbf{A} \mathbf{B} + \mathbf{B} \mathbf{A}^T \quad (\text{A12})$$

if \mathbf{B} is a rotational symmetric tensor and $\mathbf{A} = \mathbf{Q}^T \dot{\mathbf{Q}}$ is an anti-symmetric tensor.

By Eq. (A10) and (A11), we see that

$$\frac{d}{dt} \langle \tilde{\mathbf{B}} \rangle \big|_{\text{frame 1}} - \tilde{\boldsymbol{\kappa}} : \langle \tilde{\mathbf{r}} \nabla_{\tilde{\mathbf{r}}} \otimes \tilde{\mathbf{B}} \rangle \big|_{\text{frame 1}} \equiv \mathbf{Q} \left[\frac{d}{dt} \langle \mathbf{B} \rangle \big|_{\text{frame 2}} - \boldsymbol{\kappa} : \langle \mathbf{r} \nabla_{\mathbf{r}} \otimes \mathbf{B} \rangle \big|_{\text{frame 2}} \right] \mathbf{Q}^T \quad (\text{A13})$$

The rotational symmetry of the other terms follows similarly. \square

The above analysis shows that, from the perspective of the Fokker-Planck equation, the evolution dynamics retains the rotational symmetry. In particular, the term $\frac{d}{dt} \langle \tilde{\mathbf{B}} \rangle - \tilde{\boldsymbol{\kappa}} : \langle \tilde{\mathbf{r}} \nabla_{\tilde{\mathbf{r}}} \otimes \tilde{\mathbf{B}} \rangle$ provides a microscopic perspective for understanding the objective tensor derivative $\frac{\partial \mathbf{B}}{\partial t}$, which we use to construct the DNN representation of the constitutive models.

2. DNN representation

Next we establish a micro-macro correspondence via a set of encoder $\{g_i(r)\}_{i=1}^n$ (see Proposition A.4 for details) and, accordingly, a set of micro-scale tensor \mathbf{B}_i and \mathbf{c}_i , i.e.,

$$\mathbf{B}_i(\mathbf{r}) = \mathbf{f}_i(\mathbf{r})\mathbf{f}_i(\mathbf{r})^T = (g_i(r)\mathbf{r})(g_i(r)\mathbf{r})^T, \quad \mathbf{c}_i = \langle \mathbf{B}_i \rangle. \quad (\text{A14})$$

We will use $\{\mathbf{c}_i\}_{i=1}^n$ to construct the evolution dynamics (A9) via some proper DNN structure which retains the rotational invariance. In particular, we consider the fourth-order tensor $\langle \mathbf{r}\nabla_{\mathbf{r}} \otimes \mathbf{B} \rangle$ and show that the following DNN representation (see also Eq. (11) in main text) ensures the rotational symmetry of $\frac{\partial \mathbf{B}}{\partial t}$. For simplicity, the subscript i is ignored and we use \mathbf{c} to denote the set of conformation tensor $\{\mathbf{c}_i\}_{i=1}^n$.

Proposition A.3. *The following ansatz of $\langle \mathbf{r}\nabla_{\mathbf{r}} \otimes \mathbf{B} \rangle$ ensures that the dynamic of evolution of \mathbf{c} retains rotational invariance.*

$$\boxed{\langle \mathbf{r}\nabla_{\mathbf{r}} \otimes \mathbf{B} \rangle = \langle g(r)^2 \mathbf{r}\nabla_{\mathbf{r}} \otimes \mathbf{r}\mathbf{r}^T \rangle + \sum_{i=1}^6 \mathbf{G}_1^{(i)}(\mathbf{c}) \otimes \mathbf{G}_2^{(i)}(\mathbf{c})} \quad (\text{A15})$$

where \mathbf{G}_1 and \mathbf{G}_2 satisfy

$$\tilde{\mathbf{G}}_1 := \mathbf{G}_1(\tilde{\mathbf{c}}) = \mathbf{Q}\mathbf{G}_1\mathbf{Q}^T \quad \tilde{\mathbf{G}}_2 := \mathbf{G}_2(\tilde{\mathbf{c}}) = \mathbf{Q}\mathbf{G}_2\mathbf{Q}^T \quad (\text{A16})$$

Proof. Without loss of generality, we represent the fourth order tensor by the following two basis

$$\begin{aligned} & \mathbf{F}_1(\mathbf{c}) \otimes \mathbf{F}_2(\mathbf{c}) \otimes \mathbf{F}_3(\mathbf{c}) + \mathbf{F}_1(\mathbf{c}) \otimes (\mathbf{F}_2(\mathbf{c}) \otimes \mathbf{F}_3(\mathbf{c}))^{T_{\{2,3\}}} \quad \mathbf{F}_1, \mathbf{F}_3 \in \mathbb{R}^3, \mathbf{F}_2 \in \mathbb{R}^{3 \times 3} \\ & \mathbf{G}_1(\mathbf{c}) \otimes \mathbf{G}_2(\mathbf{c}) \quad \mathbf{G}_1, \mathbf{G}_2 \in \mathbb{R}^{3 \times 3}, \end{aligned} \quad (\text{A17})$$

where the super-script $T_{\{2,3\}}$ represent the transpose between the 2nd and 3rd indices; also $\mathbf{F}_1, \mathbf{F}_2, \mathbf{F}_3, \mathbf{G}_1$ and \mathbf{G}_2 satisfy the symmetry conditions

$$\begin{aligned} & \mathbf{F}_1(\tilde{\mathbf{c}}) = \mathbf{Q}\mathbf{F}_1 \quad \mathbf{F}_3(\tilde{\mathbf{c}}) = \mathbf{Q}\mathbf{F}_3 \\ & \mathbf{G}_1(\tilde{\mathbf{c}}) = \mathbf{Q}\mathbf{G}_1\mathbf{Q}^T \quad \mathbf{G}_2(\tilde{\mathbf{c}}) = \mathbf{Q}\mathbf{G}_2\mathbf{Q}^T \quad \mathbf{F}_2(\tilde{\mathbf{c}}) = \mathbf{Q}\mathbf{F}_2\mathbf{Q}^T \end{aligned} \quad (\text{A18})$$

For the term $\mathbf{G}_1(\mathbf{c}) \otimes \mathbf{G}_2(\mathbf{c})$, we have

$$\boldsymbol{\kappa} : \mathbf{G}_1(\mathbf{c}) \otimes \mathbf{G}_2(\mathbf{c}) \big|_{\text{frame2}} = \text{Tr}(\boldsymbol{\kappa}\mathbf{G}_1)\mathbf{G}_2 \quad (\text{A19})$$

and

$$\begin{aligned}
\tilde{\kappa} : \tilde{\mathbf{G}}_1(\mathbf{c}) \otimes \tilde{\mathbf{G}}_2(\mathbf{c}) \big|_{\text{frame1}} &= \left(\mathbf{Q} \boldsymbol{\kappa} \mathbf{Q}^T + \dot{\mathbf{Q}} \mathbf{Q}^T \right) : \left(\mathbf{Q} \mathbf{G}_1 \mathbf{Q}^T \otimes \tilde{\mathbf{G}}_2 \right) \\
&= \text{Tr}(\boldsymbol{\kappa} \mathbf{G}_1) \tilde{\mathbf{G}}_2 + \text{Tr}(\dot{\mathbf{Q}} \mathbf{Q}^T \mathbf{Q} \mathbf{G}_1 \mathbf{Q}^T) \tilde{\mathbf{G}}_2 \\
&= \text{Tr}(\boldsymbol{\kappa} \mathbf{G}_1) \tilde{\mathbf{G}}_2 \\
&\equiv \mathbf{Q} \left(\boldsymbol{\kappa} : \mathbf{G}_1(\mathbf{c}) \otimes \mathbf{G}_2(\mathbf{c}) \big|_{\text{frame2}} \right) \mathbf{Q}^T
\end{aligned} \tag{A20}$$

where we have used $\text{Tr}(\dot{\mathbf{Q}} \mathbf{Q}^T) \equiv 0$.

For the term $\mathbf{F}_1(\mathbf{c}) \otimes \mathbf{F}_2(\mathbf{c}) \otimes \mathbf{F}_3(\mathbf{c}) + \mathbf{F}_1(\mathbf{c}) \otimes (\mathbf{F}_2(\mathbf{c}) \otimes \mathbf{F}_3(\mathbf{c}))^{T_{\{2,3\}}}$, we have

$$\boldsymbol{\kappa} : \mathbf{F}_1(\mathbf{c}) \otimes \mathbf{F}_2(\mathbf{c}) \otimes \mathbf{F}_3(\mathbf{c}) \big|_{\text{frame2}} = \mathbf{F}_2^T \boldsymbol{\kappa} \mathbf{F}_1 \mathbf{F}_3^T \tag{A21}$$

and

$$\tilde{\kappa} : \tilde{\mathbf{F}}_1(\mathbf{c}) \otimes \tilde{\mathbf{F}}_2(\mathbf{c}) \otimes \tilde{\mathbf{F}}_3(\mathbf{c}) \big|_{\text{frame1}} = \mathbf{Q} \mathbf{F}_2^T \boldsymbol{\kappa} \mathbf{F}_1 \mathbf{F}_3^T \mathbf{Q}^T + \mathbf{Q} \mathbf{F}_2^T \mathbf{Q}^T \dot{\mathbf{Q}} \mathbf{F}_1 \mathbf{F}_3^T \mathbf{Q}^T. \tag{A22}$$

On the other hand, note that

$$\frac{d\tilde{\mathbf{B}}}{dt} \big|_{\text{frame1}} = \dot{\mathbf{Q}} \mathbf{B} \mathbf{Q}^T + \mathbf{Q} \mathbf{B} \dot{\mathbf{Q}}^T + \mathbf{Q} \frac{d\mathbf{B}}{dt} \big|_{\text{frame2}} \mathbf{Q}^T. \tag{A23}$$

To ensure the rotational symmetry of $\frac{D\mathbf{B}}{Dt}$, we have

$$\mathbf{F}_2 \equiv \mathbf{I}, \sum_{i=1}^{K_1} \mathbf{F}_1^{(i)} \otimes \mathbf{I} \otimes \mathbf{F}_3^{(i)} = \langle g(r) \mathbf{r} \otimes \mathbf{I} \otimes g(r) \mathbf{r} \rangle. \tag{A24}$$

Hence, we have

$$\begin{aligned}
\frac{d}{dt} \tilde{\mathbf{c}} - \tilde{\kappa} : \left(\sum_{i=1}^{K_1} \tilde{\mathbf{F}}_1^{(i)} \otimes \tilde{\mathbf{F}}_2^{(i)} \otimes \tilde{\mathbf{F}}_3^{(i)} + \tilde{\mathbf{F}}_1^{(i)} \otimes \left(\tilde{\mathbf{F}}_2^{(i)} \otimes \tilde{\mathbf{F}}_3^{(i)} \right)^{T_{\{2,3\}}} \right) \big|_{\text{frame1}} \\
\equiv \mathbf{Q} \left[\frac{d}{dt} \mathbf{c} - \boldsymbol{\kappa} : \left(\sum_{i=1}^{K_1} \mathbf{F}_1^{(i)} \otimes \mathbf{F}_2^{(i)} \otimes \mathbf{F}_3^{(i)} + \mathbf{F}_1^{(i)} \otimes \left(\mathbf{F}_2^{(i)} \otimes \mathbf{F}_3^{(i)} \right)^{T_{\{2,3\}}} \right) \big|_{\text{frame2}} \right] \mathbf{Q}^T
\end{aligned} \tag{A25}$$

Furthermore, using Eq. (A24), we obtain

$$\sum_{i=1}^{K_1} \mathbf{F}_1^{(i)} \otimes \mathbf{F}_2^{(i)} \otimes \mathbf{F}_3^{(i)} + \mathbf{F}_1^{(i)} \otimes \left(\mathbf{F}_2^{(i)} \otimes \mathbf{F}_3^{(i)} \right)^{T_{\{2,3\}}} = \langle g(r)^2 \mathbf{r} \nabla_{\mathbf{r}} \otimes \mathbf{r} \mathbf{r}^T \rangle. \tag{A26}$$

Accordingly, the remaining part of $\langle \mathbf{r} \nabla_{\mathbf{r}} \otimes \mathbf{B} \rangle$ is expanded by

$$\langle \mathbf{r} \nabla_{\mathbf{r}} g(r)^2 \otimes \mathbf{r} \mathbf{r}^T \rangle = \sum_{i=1}^{K_2} \mathbf{G}_1^{(i)}(\mathbf{c}) \otimes \mathbf{G}_2^{(i)}(\mathbf{c}) \tag{A27}$$

where $K_2 = 6$ due to the tensor index symmetry of 1 and 2, as well as 3 and 4.

Combining Eq. (A25), (A26) and (A27), we conclude that the decomposition

$$\langle \mathbf{r} \nabla_{\mathbf{r}} \otimes \mathbf{B} \rangle = \langle g(r)^2 \mathbf{r} \nabla_{\mathbf{r}} \otimes \mathbf{r} \mathbf{r}^T \rangle + \sum_{i=1}^6 \mathbf{G}_1^{(i)}(\mathbf{c}) \otimes \mathbf{G}_2^{(i)}(\mathbf{c}) \quad (\text{A28})$$

ensures the rotational invariance in the dynamic equation of \mathbf{c} . \square

Finally, we show that the encoder $\mathbf{f}_i(\mathbf{r})$ takes the form $g_i(|\mathbf{r}|)\mathbf{r}$ (see also Eq. (9) in the main text).

Proposition A.4. *If $\mathbf{f}(\mathbf{r}) : \mathbb{R}^3 \rightarrow \mathbb{R}^3$ satisfies*

$$\mathbf{f}(\mathbf{Q}\mathbf{r}) = \mathbf{Q}\mathbf{f}(\mathbf{r}) \quad (\text{A29})$$

for an arbitrary unitary matrix $\mathbf{Q} \in \mathbb{R}^3$, then $\mathbf{f}(\mathbf{r})$ must take the form $\mathbf{f}(\mathbf{r}) = g(r)\mathbf{r}$, where $g(r) : \mathbb{R} \rightarrow \mathbb{R}$ is a scalar function and $r = |\mathbf{r}|$.

Proof. Let \mathbf{e}_1 , \mathbf{e}_2 and \mathbf{e}_3 the basis vectors of the cartesian coordinate space. In particular, we consider $\mathbf{r} = r\mathbf{e}_1$ and denote $\mathbf{f}(\mathbf{r})$ by $(f_1(\mathbf{r}), f_2(\mathbf{r}), f_3(\mathbf{r}))$. By choosing \mathbf{Q} to be of the form

$$\mathbf{Q} = \begin{pmatrix} 0 & \cos \theta & \sin \theta \\ 1 & 0 & 0 \\ 0 & -\sin \theta & \cos \theta \end{pmatrix}, \quad (\text{A30})$$

we have

$$\mathbf{f}(\mathbf{Q}\mathbf{r}) = \begin{pmatrix} f_1(r\mathbf{e}_2) \\ f_2(r\mathbf{e}_2) \\ f_3(r\mathbf{e}_2) \end{pmatrix} = \begin{pmatrix} f_2(r\mathbf{e}_1) \cos \theta + f_3(r\mathbf{e}_1) \sin \theta \\ f_1(r\mathbf{e}_1) \\ -f_2(r\mathbf{e}_1) \sin \theta + f_3(r\mathbf{e}_1) \cos \theta \end{pmatrix} \quad (\text{A31})$$

In particular, by choosing $\theta = 0$ and $\theta = \pi$, respectively, we get $f_2(r\mathbf{e}_1) = f_3(r\mathbf{e}_1) = 0$, i.e., $\mathbf{f}(r\mathbf{e}_1) = (f_1(r\mathbf{e}_1), 0, 0)$ \square

Appendix B: The micro-scale model

The polymer solution is modeled by suspensions of dumbbell polymer molecules in explicit solvent. The bond interaction is modeled by the FENE potential, i.e.,

$$V_b(r) = -\frac{k_s}{2} r_0^2 \log \left[1 - \frac{r^2}{r_0^2} \right], \quad (\text{B1})$$

where k_s is the spring constant and $r = |\mathbf{r}|$ and \mathbf{r} is the end-end vector between the two beads of a polymer molecule. In addition, pairwise interactions are imposed between all particles (except the intramolecular pairs bonded by V_b) under dissipative particle dynamics [1, 2], i.e.,

$$\begin{aligned}\mathbf{F}_{ij} &= \mathbf{F}_{ij}^C + \mathbf{F}_{ij}^D + \mathbf{F}_{ij}^R \\ \mathbf{F}_{ij}^C &= \begin{cases} a(1.0 - r_{ij}/r_c)\mathbf{e}_{ij}, & r_{ij} < r_c \\ 0, & r_{ij} > r_c \end{cases} \\ \mathbf{F}_{ij}^D &= \begin{cases} -\gamma w^D(r_{ij})(\mathbf{v}_{ij} \cdot \mathbf{e}_{ij})\mathbf{e}_{ij}, & r_{ij} < r_c \\ 0, & r_{ij} > r_c \end{cases} \quad \mathbf{F}_{ij}^R = \begin{cases} \sigma w^R(r_{ij})\xi_{ij}\mathbf{e}_{ij}, & r_{ij} < r_c \\ 0, & r_{ij} > r_c \end{cases}\end{aligned}\tag{B2}$$

where $\mathbf{r}_{ij} = \mathbf{r}_i - \mathbf{r}_j$, $r_{ij} = |\mathbf{r}_{ij}|$, $\mathbf{e}_{ij} = \mathbf{r}_{ij}/r_{ij}$, and $\mathbf{v}_{ij} = \mathbf{v}_i - \mathbf{v}_j$, ξ_{ij} are independent identically distributed (i.i.d.) Gaussian random variables with zero mean and unit variance. \mathbf{F}_{ij}^C , \mathbf{F}_{ij}^D , \mathbf{F}_{ij}^R are the total conservative, dissipative and random forces between particles i and j , respectively. r_c is the cut-off radius beyond which all interactions vanish. The coefficients a , γ and σ represent the strength of the conservative, dissipative and random force, respectively. The last two coefficients are coupled with the temperature of the system by the fluctuation-dissipation theorem [3] as $\sigma^2 = 2\gamma k_B T$. Similar to Ref. [4], the weight functions $w^D(r)$ and $w^R(r)$ are defined by

$$\begin{aligned}w^D(r_{ij}) &= [w^R(r_{ij})]^2 \\ w^R(r_{ij}) &= (1.0 - r_{ij}/r_c)^k,\end{aligned}\tag{B3}$$

We refer to Ref. [5] for the details of the reverse Poiseuille flow simulation and the calculation of the shear rate dependent viscosity. In all the numerical experiments, the number density of the solvent particle n_s is set to be 4.0 and the number density of the polymer molecule n_p is set to be 0.5. Other model parameters are given in Tab. I.

TABLE I. Parameters (in reduced unit) of the micro-scale model of the polymer solution

	a	γ	σ	k	r_c
S-S	4.0	5.0	1.58	0.25	1.0
S-P	0.0	40.0	4.47	0.0	1.0
P-P	0.04	0.01	0.071	0.5	3.5

The training dataset is collected from micro-scale shear flow simulations of the polymer solution in a domain $[0, 20] \times [0, 20] \times [0, 20]$, with periodic boundary condition imposed in each direction. The Lees-Edwards boundary condition [6] is used to impose the shear flow rates $\dot{\gamma}$. The simulation is run for a production period of 5×10^4 with time step 10^{-3} . 36000 samples of the polymer configurations are collected with $\dot{\gamma}$ uniformly selected between $[0, 0.06]$. 32000 samples are used for training and the remaining ones are used for testing.

Appendix C: Training procedure

The constructed DeePN² model is represented by various DNNs for the encoders $\{g_i(r)\}_{i=1}^n$, stress model \mathbf{G} , evolution dynamics $\{\mathbf{H}_{1,i}\}_{i=1}^n$, $\{\mathbf{H}_{2,i}\}_{i=1}^n$ and the 4th order tensors $\{\mathcal{E}_i\}_{i=1}^n$ of the objective tensor derivatives. In particular, by choosing $g_1(r) \equiv 1$, $\mathbf{G} \propto \mathbf{H}_{2,1}$ so we do not need to train \mathbf{G} separately. The loss function is defined by

$$L = \lambda_{H_1} L_{H_1} + \lambda_{H_2} L_{H_2} + \lambda_{\mathcal{E}} L_{\mathcal{E}}, \quad (\text{C1})$$

where λ_{H_1} , λ_{H_2} and $\lambda_{\mathcal{E}}$ are hyperparameters specified later. For each training batch of m training samples, L_{H_1} , L_{H_2} , $L_{\mathcal{E}}$ are given by

$$\begin{aligned} L_{H_1} &= \sum_{i=1}^m \sum_{j=1}^n \left\| \mathbf{V}^{(i)} \hat{\mathbf{H}}_{1,j}(\hat{\mathbf{c}}_1^{(i)}, \dots, \hat{\mathbf{c}}_n^{(i)}) \mathbf{V}^{(i)T} - \langle \nabla_{\mathbf{r}}^2 \mathbf{B}_j(\mathbf{r}) \rangle^{(i)} \right\|^2 \\ L_{H_2} &= \sum_{i=1}^m \sum_{j=1}^n \left\| \mathbf{V}^{(i)} \hat{\mathbf{H}}_{2,j}(\hat{\mathbf{c}}_1^{(i)}, \dots, \hat{\mathbf{c}}_n^{(i)}) \mathbf{V}^{(i)T} - \langle \nabla V_b(r) \cdot \nabla_{\mathbf{r}} \mathbf{B}_i(\mathbf{r}) \rangle^{(i)} \right\|^2 \\ L_{\mathcal{E}} &= \sum_{i=1}^m \sum_{j=1}^n \left\| \sum_k \mathbf{V}^{(i)} \hat{\mathbf{E}}_{1,j}^{(k)}(\hat{\mathbf{c}}_1^{(i)}, \dots, \hat{\mathbf{c}}_n^{(i)}) \mathbf{V}^{(i)T} \otimes \mathbf{V}^{(i)} \hat{\mathbf{E}}_{2,j}^{(k)}(\hat{\mathbf{c}}_1^{(i)}, \dots, \hat{\mathbf{c}}_n^{(i)}) \mathbf{V}^{(i)T} \right. \\ &\quad \left. - \langle \mathbf{r} \nabla_{\mathbf{r}} g(r)^2 \otimes \mathbf{r} \mathbf{r}^T \rangle^{(i)} \right\|^2, \end{aligned} \quad (\text{C2})$$

where $\|\cdot\|^2$ denotes the total sum of squares of the entries in the tensor. $\mathbf{V}^{(i)}$ is the matrix composed of the eigenvectors of $\mathbf{c}_1 = \langle \mathbf{r} \mathbf{r}^T \rangle$ of the i -th sample.

Furthermore, we note that \mathbf{c} , \mathbf{H}_1 , \mathbf{H}_2 , \mathbf{E}_1 and \mathbf{E}_2 are all symmetric. Accordingly, the DNN inputs are composed of the upper-triangular parts of the \mathbf{c} and the outputs are the upper-triangular parts of the representation tensors. Specifically, $\{g_j\}_{j=1}^n$, $\{\mathbf{H}_{1,j}\}_{j=1}^n$, $\{\mathbf{H}_{2,j}\}_{j=1}^n$, $\{\mathbf{E}_{1,j}, \mathbf{E}_{2,j}\}_{j=1}^n$ are represented by the 8-layer fully-connected DNNs. The number of neurons in the hidden layers are set to be (120, 120, 120, 120, 120, 120), (300, 300, 400, 400, 300, 300),

(400, 600, 600, 600, 600, 400), (300, 300, 300, 300, 300, 300), respectively. The activation function is taken to be the hyperbolic tangent.

The DNNs are trained by the Adam stochastic gradient descent method [7] for 400 epochs, using 75 samples per batch size. The initial learning rate is 1.8×10^{-4} and decay rate is 0.8 per 9000 steps. The hyper-parameters λ_{H_1} , λ_{H_2} and $\lambda_{\mathcal{E}}$ are chosen in the following two ways. In the first setup, we set them to be constant throughout the training process, e.g., $\lambda_{H_1} = \lambda_{H_2} = \lambda_{\mathcal{E}} = 1/3$. In the second setup, the hyper-parameters are updated every N_{λ} epochs by

$$\lambda_{H_1} = \frac{\tilde{L}_{H_1}}{\tilde{L}_{H_1} + \tilde{L}_{H_2} + \tilde{L}_{\mathcal{E}}}, \quad \lambda_{H_2} = \frac{\tilde{L}_{H_2}}{\tilde{L}_{H_1} + \tilde{L}_{H_2} + \tilde{L}_{\mathcal{E}}}, \quad \lambda_{\mathcal{E}} = \frac{\tilde{L}_{\mathcal{E}}}{\tilde{L}_{H_1} + \tilde{L}_{H_2} + \tilde{L}_{\mathcal{E}}}, \quad (\text{C3})$$

where $\tilde{L}_{(\cdot)}$ denotes the mean of the loss during the past N_{λ} epochs. For the present study, both approaches achieve a loss L smaller than 1×10^{-4} and the root of relative loss less than 1.6×10^{-2} . More sophisticated choices of λ_{H_1} , λ_{H_2} and $\lambda_{\mathcal{E}}$ as well as other formulation of L will be investigated in future work.

Appendix D: Computational cost

We consider two dynamic processes: relaxation to quasi-equilibrium and the development of the reverse Poiseuille flow. For relaxation to quasi-equilibrium, the micro-scale simulation is conducted in a domain $[0, 10] \times [0, 10] \times [0, 10]$ (in reduced unit), which is mapped into a volume unit in the continuum DeePN², Hookean and FENE-P models. All simulations are run for a production period of 360 (in reduced unit). For the case of the reverse Poiseuille flow, the microscale simulation is conducted in a domain $[0, 40] \times [0, 80] \times [0, 40]$. The simulations of the continuum DeePN², Hookean, and FENE-P models are conducted by mapping the domain into 20 volume units along y direction. All simulations are run for a production period of 550. The computational cost for both systems is reported in Tab. II. All simulations are performed on Michigan State University HPCC supercomputer with Intel(R) Xeon(R) CPU E5-2670 v2.

We note that the size of the volume unit is chosen empirically in the continuum models of the flow systems considered in the present work. Our sensitivity studies show that the numerical results of the DeePN² model agree well with the full MD when the average number of polymer within a unit volume is greater than 200. For all the cases, the computational

TABLE II. Computational cost (in CPU-second) using the MD model and the continuum DeePN², FENE-P and Hookean models.

	MD	DeePN ²	FENE-P	Hookean
Quasi-equilibrium	2.35×10^4	4.1	0.56	0.51
Reverse Poiseuille flow	9.24×10^6	85.6	10.2	9.7

cost of the DeePN² model is less than 0.05% of the computational cost of the full MD simulations and less than 10 times the cost of empirical continuum models.

-
- [1] P. J. Hoogerbrugge and J. M. V. A. Koelman, Europhys. Lett. **19**, 155 (1992).
 - [2] R. D. Groot and P. B. Warren, Journal of Chemical Physics **107**, 4423 (1997).
 - [3] P. Espanol and P. Warren, Europhysics Letters **30**, 191 (1995).
 - [4] H. Lei, B. Caswell, and G. E. Karniadakis, Phys. Rev. E **81**, 026704 (2010).
 - [5] H. Lei, X. Yang, Z. Li, and G. E. Karniadakis, J. Comput. Phys. **330**, 571 (2017).
 - [6] A. W. Lees and S. F. Edwards, Journal of Physics C **5**, 1921 (1972).
 - [7] D. Kingma and J. Ba, International Conference on Learning Representations (ICLR) (2015).